

Reconstruction of Three-Dimensional Dendritic Structures based on the Investigation of Microsegregation Patterns

J. Domitner^{1)*}, A. Kharicha²⁾, M. Grasser²⁾, and A. Ludwig^{1,2)}

¹⁾ Christian Doppler Laboratory for Multiphase Modeling of Metallurgical Processes, University of Leoben, Austria

²⁾ Chair of Simulation and Modeling of Metallurgical Processes, University of Leoben, Austria

* Corresponding author; e-mail: josef.domitner@unileoben.ac.at

The shape of growing dendrites during the solidification of cast steel depends on many different parameters. This includes the casting technique, the applied cooling conditions or the casting geometry. Alloying elements such as carbon, silicon or manganese have a major influence on the solidification behaviour and therefore on the morphology of the growing dendrites. In this paper, a method is presented which enables the reconstruction of three-dimensional dendritic structures by using concentration maps of a certain alloying element. For this purpose, a sample of a conventionally produced St52 continuous casting steel has been investigated. To determine the required two-dimensional maps, an electron probe microanalyzer (EPMA or "microprobe") with wavelength dispersive spectrometers (WDS) has been used. After the EPMA measurements, a commercial software tool has been utilized to process the concentration maps to three-dimensional structures. This processing includes an iterative numerical method which allows estimating the curvature effect on the measured concentration patterns and therefore on the dendritic shape.

Keywords: dendritic structures, 3D-reconstruction, microprobe (EPMA), microsegregation, curvature

Submitted on 2 February 2010, Accepted on 16 April 2010

Introduction

Nowadays several investigation methods are available to reconstruct three-dimensional shapes. Their application depends on the required purpose. In the field of metallurgy, computed tomography (CT) has become a sophisticated method to visualize the structure of metals [1]. To gain accurate results using this method for volumetric analysis, sufficient density differences within the sample are required. CT also allows the examination of the surface topography of a sample. As an example for such measurements, the surface of a partially solidified dendritic structure after decanting the remaining interdendritic melt is illustrated in **Figure 1**. Another possibility to produce three-dimensional metallic structures is the serial sectioning method. Several variations of this method have a long tradition in the field of metallography [2]. The reconstruction is always based on a set of light microscopy images taken from polished surface areas at the same lateral sample position, but at different depths. Today the sectioning and polishing of the investigated samples as well as the image acquisition is done semi-automated [3, 4]. It is obvious that this method needs adequate differences in contrast between dendritic and interdendritic areas. Many non-ferrous alloys provide such contrast after solidification, but occasionally this can also be achieved by etching the sample's surface.

Both described methods have one main disadvantage: only the shape of the final solidified structure can be reconstructed. Therefore, it is not possible to visualize the shape of the growing dendrites during the solidification process. To gain information about the changing structure with ongoing solidification, it is necessary to focus on a

detectable parameter which varies with the volume of solid fraction. For the reconstruction method presented here, this parameter is the concentration of the alloying element manganese (Mn) inside a solidified metal sample. The Mn-concentration can be measured at room temperature after solidification has been completed.

When cooling down from the liquid, dendritic crystals form with different composition to the melt. The amount of a certain alloying element inside such crystals depends on its specific segregation behaviour in the presence of iron and other elements. Hence, it can be enriched or reduced in the solid phase in relation to its average content in the melt [5]. For instance, the concentration of Mn increases with advancing solidification. Considering that the change in concentration of a certain alloying element is more or less proportional to the increasing fraction of solid, the concentration distribution at room temperature within a dendrite must approximate the distribution during the growth of the solid phase. Neglecting Ostwald ripening and diffusion within the solid, the determination of the local concentration allows an inference to the growth of the dendritic structure.

The idea behind the presented reconstruction method is to measure the concentration pattern of a certain alloying element at a defined sample position. The sample is sectioned several times and at each layer the concentrations are measured at the same horizontal position. Afterwards, the measured patterns can be merged to a three-dimensional structure by connecting concentrations which have a predefined value. A similar method is used at microscale level, where the sample material is removed with a focussed ion beam (FIB) and the concentrations are measured by an energy dispersive spectrometer (EDS) [6].

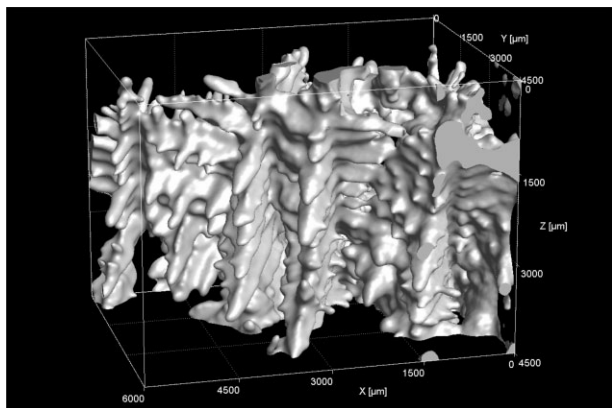


Figure 1. 3D-reconstruction of steel dendrites; computed tomography measured at the ÖGI, Leoben.

Experimental Methods

Embedding the sample. The sample used for the investigations was taken from an industrially produced St52 continuous casting slab. The position close to the slab's surface (shown in **Figure 2**) was chosen to achieve an oriented columnar dendritic structure. The final size of the investigated sample area was about 3×3 mm in square.

For microprobe analysis it is necessary to guarantee the conductivity of electricity between the sample holder and the mounted specimen. To achieve this, non-conductive samples and embedding materials (e.g. minerals, conventional plastics) are sputtered with a graphite coating inside a vacuum chamber. A possibility for conductive samples (e.g. metals) is to embed them directly into a conductive material, like a metallic alloy. In the recent study a eutectic tin-bismuth-alloy with a melting point below 150°C was used for this purpose [7]. By applying this method, the conductivity of electricity required for the measurements is ensured inside the complete volume of both, sample and embedding mass, and not only on their upper surface. This is a great advantage, especially if the surface layer is removed several times between the measurements. A further advantage is that the metallic embedding alloy does not tend to evaporate and to contaminate the vacuum chamber of

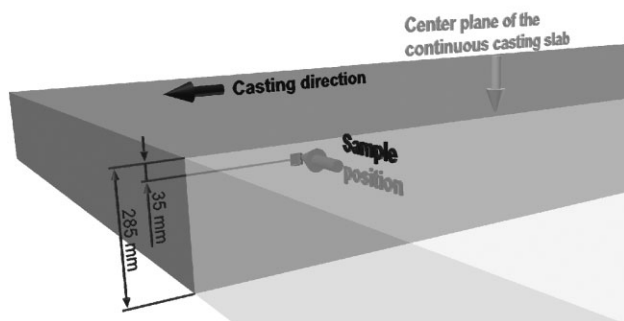


Figure 2. Position of the investigated sample inside a continuous casting slab.

the microprobe, if the electron beam passes it during the measurement. The mechanical resistance of the embedding material to the beam is very important, since during the measurement procedure the embedding was also analysed in the vicinity of the sample. The low X-ray intensities detected there produced sharp border lines to the comparatively high intensities inside the investigated sample area. Therefore an exact alignment of the measured maps was possible by orienting them along the detected sample edges. **Figure 3** shows the investigated St52 sample, completely embedded in the SnBi-alloy.

Polishing the sample. To achieve sufficient results with quantitative microprobe measurements, it was necessary that the examined surface area was well polished. To prepare the sample for the measurements, the embedded sample shown in **Figure 3** was positioned in a semi-automated polishing machine where the material was removed in two steps: For the first step a mono-crystalline $3\ \mu\text{m}$ diamond suspension on a satin woven natural silk cloth was used. This suspension allows fast material removal. The second step consists in a polishing performed with a mono-crystalline $1\ \mu\text{m}$ diamond suspension on a porous neoprene cloth. During the whole procedure sufficient alcohol-based lubricant liquid was added to cover the used polishing cloths with a thin liquid film. The removed layer thickness from the surface of the sample was $25\ \mu\text{m}$ ($\pm 3\ \mu\text{m}$), checked by control surveys with a digital indicating calliper which allows theoretically a measurement resolution of $1\ \mu\text{m}$. Altogether, the concentration of Mn in five different layers was measured.

Microprobe measurements. All concentration measurements presented in this paper were carried out using the electron probe microanalysis. This is an efficient method, which allows the non-destructive determination of chemical compositions at solid materials like minerals, metals, biogenic matter, etc.. At the electron probe microanalyzer (EPMA), a high energetic focussed electron beam impacts the sample's surface and generates X-rays from a small volume below the interaction spot. These X-rays are characteristic for the elements inside the investigated

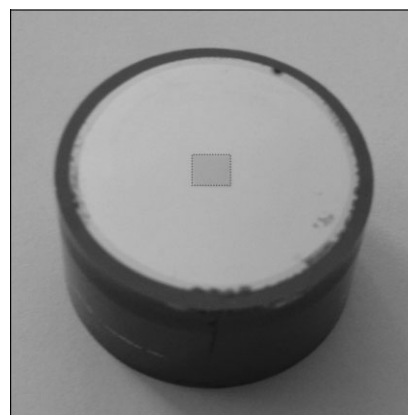


Figure 3. Embedded St52 sample (grey square in the centre).

specimen. The higher the measured X-ray intensity for a certain element, the larger is its content within the sample. To get a quantitative result for the chemical concentration of an element, the measured intensity must be compared with the value of a standard material which is well known in its composition. Then C_S is calculated with Eq. (1) [8]:

$$C_S = C_{STD} \cdot \frac{I_S}{I_{STD}} \cdot ZAF \quad (1)$$

In the above-mentioned equation, C_S is the unknown concentration of a certain element at the investigated sample position, C_{STD} is the known concentration of the same element inside the standard, I_S stands for the measured X-ray intensity of this element in the sample and I_{STD} for its measured X-ray intensity in the standard. The *ZAF*-factor takes into account the influence of the atomic numbers on the calculated concentration value as well as effects of absorption and fluorescence.

The investigation of the St52 sample was conducted using wavelength dispersive X-ray spectrometers (WDS) at a JEOL 8200 microprobe with the basic settings from **Table 1**. It takes approximately 16 hours to measure the concentrations of Mn with these settings. The result of a WDS-measurement is an “intensity map”, wherein each pixel represents a small area with a corresponding value for the measured X-ray intensity. To obtain values for the concentration of a specific element, it is necessary to quantify the intensity map with a known standard as shown in Eq. (1). Normally this can be achieved directly using the software implemented in the microprobe device; the quantified map is then called “concentration map”. For the reconstruction method presented here, five maps (taken from different depths in the sample) had been measured. For each pixel with a size of $5 \times 5 \mu\text{m}$, the value of the corresponding Mn-concentration was clearly determined. **Figure 4** shows one of the original concentration maps for Mn, measured at the JEOL 8200 microprobe.

Processing of the Concentration Maps

The commercial software package MATLAB® was used to process the concentration maps with the following procedure.

Table 1. Basic settings of the JEOL 8200 microprobe.

Analysed element:	Mn
Analysing crystal:	LIFH
Acceleration voltage:	15 kV
Beam current:	250 nA
Preset value for the probe diameter:	0 μm (focussed)
Dwell time per measurement point:	120 ms
Interval between measured points:	5 μm (in x- and y-direction)
Number of measured points:	660 × 660

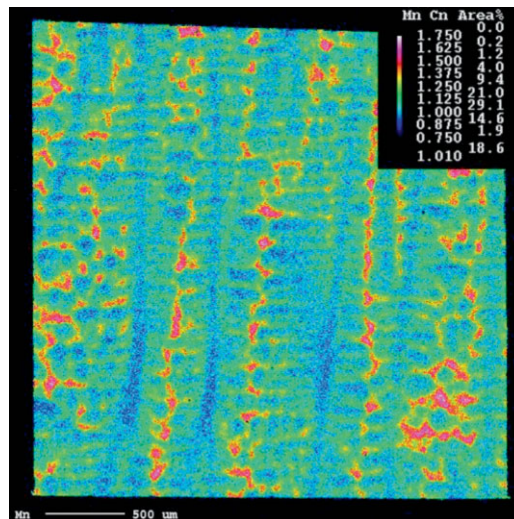


Figure 4. Typical concentration map for Mn in steel measured with wavelength dispersive X-ray spectrometers (WDS).

Image filtering. As depicted in Figure 4, large jumps in concentration between adjacent pixels can appear locally which make the reconstruction of smooth iso-concentration lines or faces impossible. Therefore it was necessary to smooth these undesirable concentration jumps before reconstructing the three-dimensional dendritic structure. This smoothing procedure, also called “image filtering”, was achieved in two steps.

If the electron beam passes a non-metallic inclusion inside the investigated sample, the detected X-ray intensity can be up to ten times higher than the expected intensity found in the surrounding area. In contrast, if there is a hole in the investigated surface, it may lead to an abrupt decay of intensity at this location. Therefore the concentration values calculated from the measured intensities may become extremely high or low, due to an inclusion or a hole respectively. To remove such extreme intensity or concentration peaks also known as “salt and pepper noise”, a median filter [9] was applied on the present concentration maps. This filter is defined as:

$$C_{S'}(x, y) = \text{median}\{C_S(x + i, y + j)\}_{(i,j) \in R_{x,y}} \quad (2)$$

In Eq. (2), $C_{S'}(x, y)$ is the new concentration value for a certain pixel at the Cartesian map coordinates x and y . It is calculated as the median of the original concentration values $C_S(x + i, y + j)$ at the map coordinates $x + i$ and $y + j$. The local coordinates i and j only exist inside the predefined filter area $R_{x,y}$, which surrounds the pixel.

The application of the median filter removed only the undesired peak values. Nevertheless, the resulting concentration map was not very smoothed compared to the original one and differences between single values at adjacent pixels still existed. Therefore a Gaussian filter was applied to the median filtered maps in a second step. It led to a blurring effect and smooth transitions in concentration were

achieved. The Gaussian filter is expressed by the following two equations [10]:

$$C_{S''}(x, y) = \sum_{(i,j) \in R_{x,y}} C_{S'}(x+i, y+j) \cdot G(i, j) \quad (3)$$

and

$$G(i, j) = e^{-\frac{i^2+j^2}{2\sigma^2}} \quad (4)$$

In Eq. (3), $C_{S''}(x, y)$ is the new concentration value for a certain pixel at the Cartesian map coordinates x and y . $R_{x,y}$ is the filter area surrounding this pixel and $C_{S'}(x+i, y+j)$ are the median filtered concentration values at the map coordinates $x+i$ and $y+j$. The two-dimensional Gaussian weighting function $G(i, j)$ with the local coordinates i and j is only valid inside of $R_{x,y}$. In Eq. (4), the standard deviation σ defines the width of $G(i, j)$. To process the present concentration maps, the size of $R_{x,y}$ was chosen with 9×9 pixels in square for the median as well as for the Gaussian filter. To achieve a sufficient smoothing effect, σ was set to 2 pixels.

Alignment of the concentration maps. After image filtering, all concentration values of the five maps were stored in a three-dimensional matrix which included five layers. Each single map was allocated to one of these layers. It was necessary to shift and to rotate them to a specific position, so that the maps lay exactly one upon each other. The required alignment of the maps was achieved by adjusting them along their outlines which were visible due to the large difference in the concentration of Mn between the sample and the embedding material. After preparing the concentration matrix, its outer areas were cut off to ensure, that the values inside actually belong to the investigated sample and not to the surrounding embedding material. This operation reduced the matrix to a size of $550 \times 550 \times 5$ values, which corresponds to physical dimensions of $2750 \times 2750 \times 100 \mu\text{m}$. To obtain the three-dimensional dendritic structure, all entries which contain a preset concentration value of Mn inside the matrix were connected with iso-surfaces. But this immediate connection does not include the effect of curvature on the processed concentration values.

Considering the effect of curvature. In solidification processes, it is known that the free enthalpy of the solid phase increases with decreasing diameter of the solid particles. Assuming a constant free enthalpy of the liquid phase, this phenomenon leads to a

reduction of the liquidus and solidus temperatures related to the curvature of the solid surface [11]. This temperature drop ΔT_K caused by the curvature can be defined as

$$\Delta T_K = \Gamma \cdot K \quad (5)$$

K represents the local surface curvature and Γ is the material dependent Gibbs-Thomson coefficient. Focussing on steel, a commonly used value for Γ is $0.19 \text{ K} \mu\text{m}$ [11, 12]. If we assign this relation to complex shaped dendritic structures, it is obvious that ΔT_K can be negative for negative values of K . Therefore, this leads to ascending liquidus and solidus temperatures, which typically occur at the indentations between the secondary dendrite arms for instance. The relationship between the temperature drop ΔT_K and the concentration differences ΔC_K^i due to curvature can be written as

$$\Delta T_K = - \sum_i m^i \cdot \Delta C_K^i, \quad (6)$$

where the proportionality factor m^i characterizes the slope of the solidus line in the equilibrium phase diagram for a certain alloying element i . Note that in principle all alloying elements of the investigated steel could have an influence on ΔT_K . However, compared with Mn, most of these elements show only low concentration differences in their corresponding microprobe maps. Therefore it can be assumed that Mn has the main influence on ΔT_K , which then can be approximated as

$$\Delta T_K \approx -m^{\text{Mn}} \cdot \Delta C_K^{\text{Mn}}. \quad (7)$$

For the investigations described here in this paper, m^{Mn} was estimated by the commercial software package Thermo-Calc[®] Classic, database SSOL4 [13]. The thermodynamic calculations were based on the chemical composition of the St52 steel, given in **Table 2**. For the calculations, the elements C and N were assumed to be fast diffusing. Since the alloying element of major interest was Mn, which generally has a low diffusion tendency in solid steel, a Scheil calculation was performed instead of an equilibrium state calculation. For elements with poor solid-state diffusivity, the Scheil method delivers results which are closer to real solidification conditions. The results generated by Thermo-Calc[®] Classic and post-processed with MATLAB[®] (**Figure 5** and **Figure 6**) show that the slope m^{Mn} varies during ongoing solidification and therefore with changing weight fraction of Mn (**Figure 6**). As a suitable linear approximation, the constant values of $-90 \text{ K}/\%$ for the BCC phase and $-34 \text{ K}/\%$ for the FCC phase are utilized for further calculations.

Table 2. Chemical composition of the investigated St52 steel in wt.%.

C	Si	Mn	P	S	Cr	Ni	Cu	Mo	Ti	V	Nb	W	N	Al
0.182	0.360	1.170	0.008	0.001	0.170	0.270	0.170	0.002	0.002	0.001	0.022	0.015	0.008	0.036

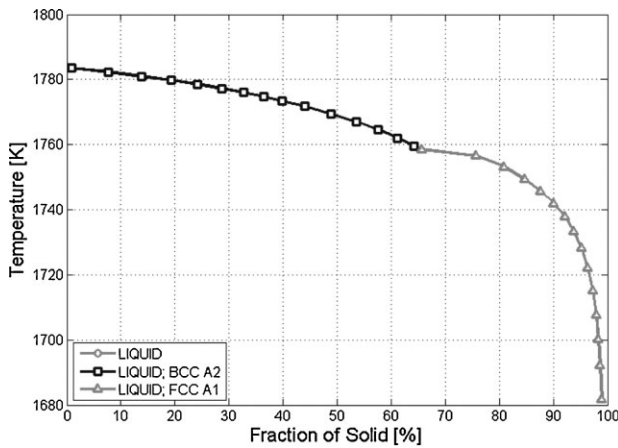


Figure 5. Occurrence of the main phases calculated with Thermo-Calc® Classic.

Now, combining both Eq. (5) and Eq. (7), gives an expression which relates the concentration difference ΔC_K^{Mn} to the curvature K of the dendritic surface:

$$\Delta C_K^{Mn} = - \frac{\Gamma \cdot K}{m^{Mn}} \tag{8}$$

Finally, Eq. (8) can be used to calculate the curvature influence on the measured and filtered concentration values $C_{S''}$ as

$$C_{S^*} = C_{S''} + \Delta C_K^{Mn} = C_{S''} - \frac{\Gamma \cdot K}{m^{Mn}} \tag{9}$$

with

$$K = \text{div} \frac{\text{grad } C_{S^*}}{\|\text{grad } C_{S^*}\|} \tag{10}$$

The gradient of C_{S^*} was calculated by using a central difference scheme, whereas it was only approximated by a first order method at the boundary layers. To reduce the influence of these boundary values, the number of layers

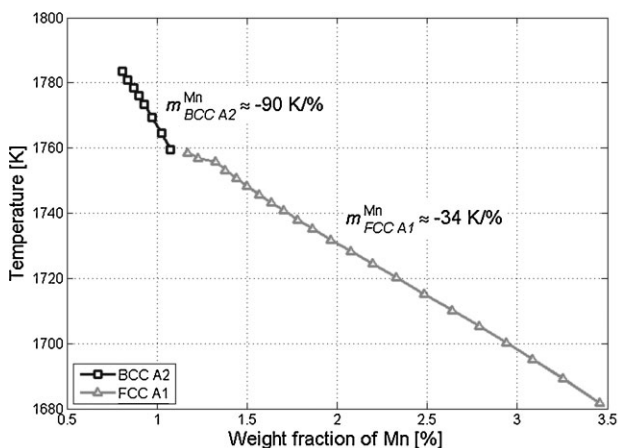


Figure 6. Weight fraction of Mn inside the BCC and FCC phases calculated with Thermo-Calc® Classic.

was numerically increased by a cubic interpolation between the concentrations in one direction. So the original matrix containing $550 \times 550 \times 5$ concentration values became a larger matrix with $550 \times 550 \times 9$ values. This reduced the distance between each layer from $25 \mu\text{m}$ to $12.5 \mu\text{m}$. Generally it can be mentioned, that the higher the number of available layers, the better are the achieved calculation results.

It is very important to understand that the curvature K is related to the unknown variable C_{S^*} . Since the present problem is highly non-linear, an iterative approach is necessary for the calculation of C_{S^*} :

$$C_{S^*}^{\nu+1} = \alpha \cdot \left(C_{S''} - \frac{\Gamma \cdot K(C_{S^*}^{\nu})}{m^{Mn}} \right) + (1 - \alpha) \cdot C_{S^*}^{\nu} \tag{11}$$

The index ν in Eq. (11) counts the number of executed iterations. The initial guess is taken with $C_{S^*}^0 = C_{S''}$. In practice, if the value for ΔC_K^{Mn} reaches the order of $C_{S''}$, the solution of Eq. (11) shows an unstable behaviour. This may happen if the value of m^{Mn} changes during calculation. To reduce this unfavourable effect, a relaxation factor α was introduced, which was set to a value of 0.1. The iterative calculation was running until the residual R^{ν} , defined in Eq. (12), reached a small and constant value ($R^{\nu} \approx R^{\nu+1} \approx \dots \approx R^{\nu+\infty} \ll 1$).

$$R^{\nu} = \sum_{x,y} \frac{\left(C_{S^*}^{\nu} + \frac{\Gamma \cdot K(C_{S^*}^{\nu})}{m^{Mn}} - C_{S''} \right)^2}{C_{S''}^2} \tag{12}$$

In the following, two examples are given to illustrate the change in shape of a surface by using the presented method. These examples were chosen to check, if a given shape could be recovered by the iterative curvature correction described with Eq. (11). For the first example, an idealized parabolic dendrite tip was produced by connecting a certain concentration value inside an artificially generated concentration field. This tip, shown in **Figure 7a**, represents the original shape to be recovered. An additional concentration field, related to the curvature of the artificially generated one, was calculated by using Eq. (8). Afterwards, both fields were superimposed. This changed the original concentration values and therefore the surface of the idealized dendrite tip, as depicted in **Figure 7b**. By applying the iterative calculation method of Eq. (11) ($\Gamma = 0.19 \text{ K} \mu\text{m}$, $m^{Mn} = -0.1 \text{ K}/\%$, $\alpha = 0.1$) to the modified concentration field of Figure 7b, it was possible to obtain the original parabolic dendrite tip, as shown in **Figure 7d**. To achieve this, 50 iterations were necessary. A second example representing a more complex surface is shown in **Figure 8**.

The same procedure was applied to the concentration matrix generated by the described pre-processing (filtering, smoothing and aligning) of the microprobe data. The aim was to calculate the change of the concentration field and therefore of the dendritic shape due to the curvature effect on the concentrations. Nevertheless, the iso-surface generated from the experimental data is much more complex than those of the two examples shown before.

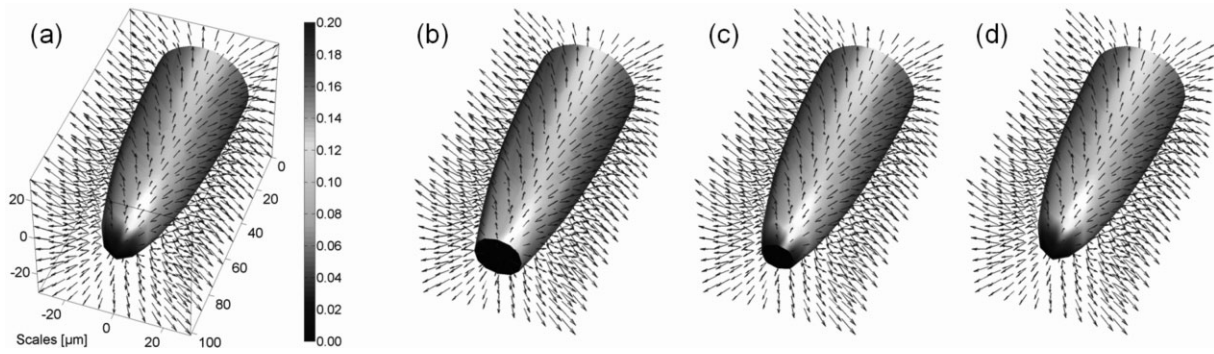


Figure 7. Example for recovering a given shape by iterative curvature correction; (a) given shape of an artificial dendrite tip, (b) shape after superimposing a concentration field related to the curvature - initial state for the iterative calculation, (c) shape after 10 iterations, (d) shape after 50 iterations. The shadings on the surfaces represent the curvature [$1/\mu\text{m}$], the arrows show the concentration gradient.

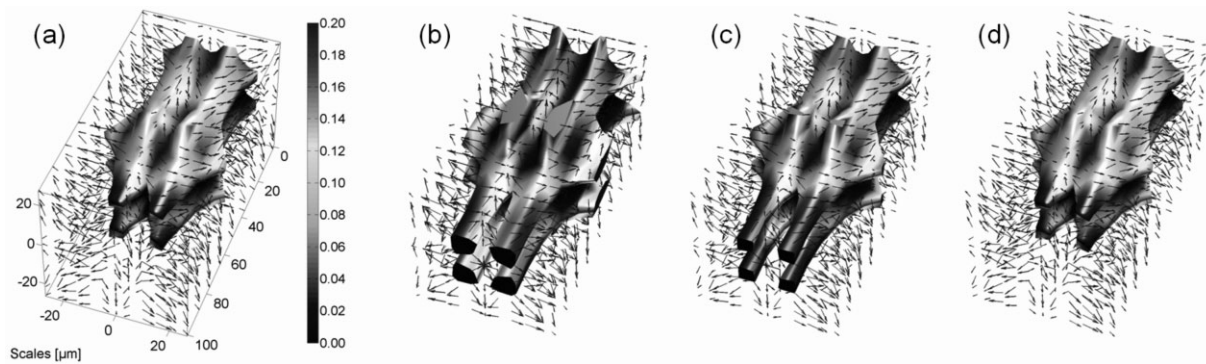


Figure 8. Example for recovering a given complex shape by iterative curvature correction; (a) given shape of four artificial dendrites, (b) shape after superimposing a concentration field related to the curvature - initial state for the iterative calculation, (c) shape after 10 iterations, (d) shape after 50 iterations. The shadings on the surfaces represent the curvature [$1/\mu\text{m}$], the arrows show the concentration gradient.

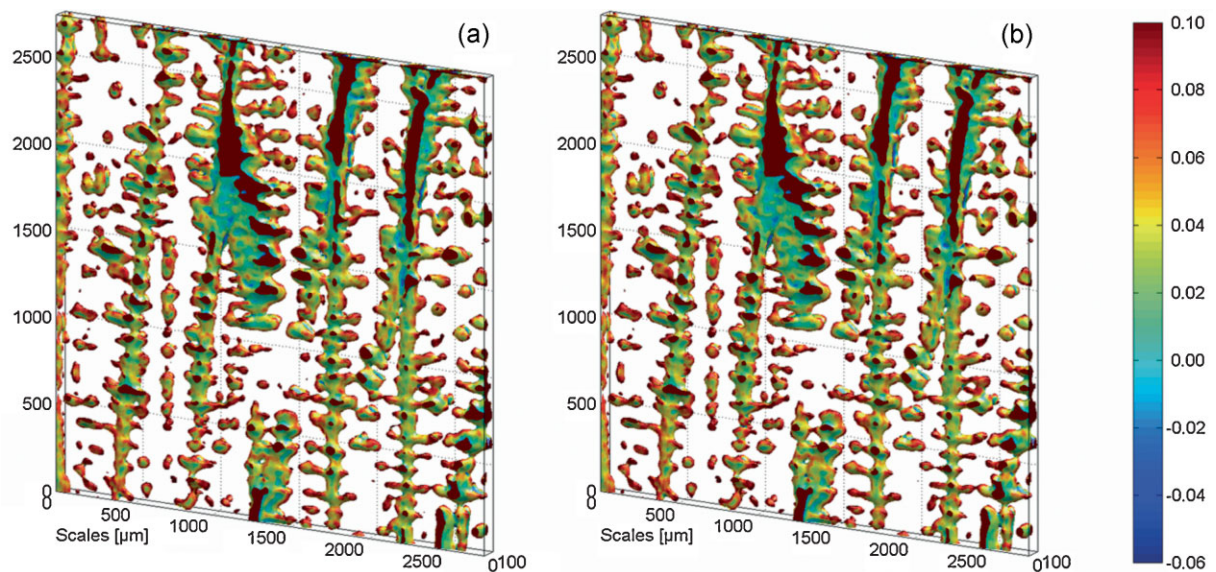


Figure 9. Dendritic structure before (a) and after (b) considering the curvature effect on the concentration field; the colours on the surfaces represent the local curvature [$1/\mu\text{m}$].

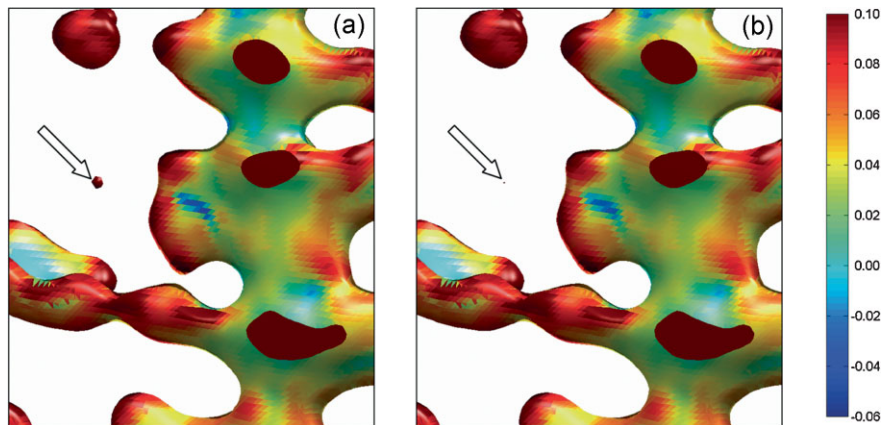


Figure 10. Detail of the dendritic structure before (a) and after (b) considering the curvature effect on the concentration field; the colours on the surfaces represent the local curvature [$1/\mu\text{m}$]. The arrow shows a small, strongly curved object which disappears by applying the iterative calculation method.

Results and Discussion

Figure 9 shows the entire dendritic structures before (Figure 9a) and after (Figure 9b) considering the curvature effect on the concentrations. Both structures were generated by connecting a concentration value of 1.00% Mn. Since there are no significant differences between the left and the right figure, it seems that the curvature has no relevant effect on the dendritic structure of the investigated St52 steel. But on closer inspection, it can be seen that small objects with a high curvature shrink and even may disappear, as shown in **Figure 10**. However, the appearance of isolated objects is not totally prevented by considering the effect of curvature on the measured concentration field. At the current state of investigations, the reason of this phenomenon is unknown. Some of these objects are secondary and tertiary dendrite arms, reaching from outside into the reconstructed volume. But some of them might also be caused by diffusion effects which are not taken into consideration or by an over- or

underestimation of m^{Mn} . Nevertheless, such isolated “concentration isles” also appeared in the results of phase-field simulations performed by Warren and Boettinger [14, 15].

Finally, to get the desired dendritic structure based on the corrected concentration matrix, all entries which contain a preset concentration value of Mn were connected with iso-surfaces. Depending on the change of this value, it is possible to illustrate different stages of microsegregation during the dendritic growth, as shown in **Figure 11** below. The entire structure depicted has overall dimensions of $2750 \times 2750 \times 100 \mu\text{m}$. It gives an appropriate approximation of the shape of the growing dendrites with advancing solidification. However, to get more precise three-dimensional reconstructions for different fractions of solid, the effect of a non-uniform temperature field on the microsegregation pattern as well as the alteration of microsegregation due to ripening processes and to the diffusivity within the solid state have to be considered. These are ongoing tasks.

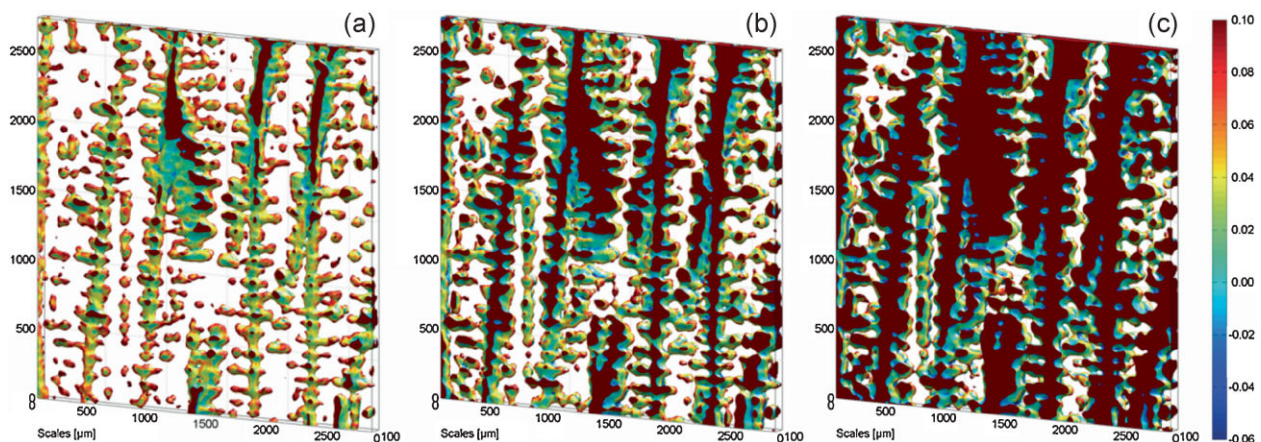


Figure 11. Different fractions of solid depending on the predefined concentration values of manganese; the colours on the surfaces represent the local curvature [$1/\mu\text{m}$]. The dark red plane surfaces are the boundaries of the structures. (a) 1.00% Mn, (b) 1.05% Mn, (c) 1.10% Mn.

Conclusions

A method to reconstruct the three-dimensional shape of dendritic structures is presented in this paper. This reconstruction method based on serial sectioning of the investigated sample uses a set of two-dimensional microprobe concentration maps which show the quantitative distribution of Mn at the investigated surface area. These maps are generated by an electron probe microanalyzer (EPMA) equipped with wavelength dispersive spectrometers (WDS). The WDS-device allows the accurate quantification of element concentrations at each measured point. After the microprobe measurements, different image filters are applied to the created maps to prepare them for further processing. The concentration values of all filtered maps are merged in a three-dimensional matrix and then the curvature of this concentration field is calculated with an iterative procedure. Based on the determined curvatures a correction of the original concentration field is possible. Finally all pixels which have a certain predefined concentration value are connected with an iso-surface. Since the concentration of the investigated alloying element (Mn) within the solid increases during solidification, the surface approximates the dendritic morphology at a certain solidification stage. Provided that Ostwald ripening is ignored, it is possible to visualize the growth of the dendritic structure by increasing the predefined concentration value.

Acknowledgements

This work was performed within the Competence Centres for Excellent Technologies (COMET) program in cooperation with the Materials Center Leoben Forschung GmbH (MCL). It was sponsored by the Ministry of Transport, Innovation and Technology (BMVIT), the Ministry of Economy, Family and Youth (BMWFJ) as well as the province of Styria and managed by the Austrian Research Promotion Agency (FFG). Thanks go to these institutions for providing the financial support of the current COMET project.

The authors would also like to thank the industrial partner voestalpine Stahl GmbH, voestalpine Stahl Donawitz

GmbH & Co KG and Siemens VAI Metals Technologies GmbH & Co for their contributions to this project. Thanks go to Mrs. Judith Fluch from voestalpine Stahl GmbH as well as to Mrs. Federica Zaccarini and Mr. Helmut Mühlhans from the University of Leoben for supporting the microprobe measurements. Thanks also go to Mr. Siegfried Schider from the Materials Center Leoben Forschung GmbH for the excellent preparation of the investigated sample. Special thanks are due to the Austrian Foundry Institute (ÖGI) in Leoben for providing the computed tomography measurement.

References

- [1] D. Fuloria, P. D. Lee, D. Bernard: *Materials Science and Engineering A*, 494 (2008), 3–9.
- [2] M. V. Kral, M. A. Mangan, G. Spanos, R. O. Rosenberg: *Materials Characterization*, 45 (2000), 17–23.
- [3] J. Alkemper, P. W. Voorhees: *Journal of Microscopy*, 201 (2001), No. 3, 388–394.
- [4] J. Madison, J. E. Spowart, D. J. Rowenhorst, T. M. Pollock: *JOM*, 60 (2008), No. 7, 26–30.
- [5] S. Ilie, H. Preßlinger, P. Reisinger, M. Mayr, K. Eitzelsdorfer: *Steel Research International*, 78 (2007), No. 4, 327–332.
- [6] M. Schaffer, J. Wagner, B. Schaffer, M. Schmied, H. Mulders: *Ultramicroscopy*, 107 (2007), 587–597.
- [7] M. Mayr: *Metallic Embedding of Samples for EPMA*. Internal working instruction, voestalpine Stahl GmbH, Linz (2003).
- [8] X. Llovet: *Quantitative analysis with the electron microprobe*. UZAG-Workshop (2008). University of Leoben, Austria.
- [9] R. C. Gonzalez, R. E. Woods, S. L. Eddins: *Digital Image Processing Using MATLAB*. Pearson Prentice Hall: Upper Saddle River (2004). ISBN 978-0-13008-519-1.
- [10] W. Burger, M. J. Burge: *Digitale Bildverarbeitung*. Springer: Berlin, Heidelberg, New York (2006). ISBN 978-3-540-30940-6.
- [11] W. Kurz, D. J. Fisher: *Fundamentals of Solidification*. Trans Tech Publications: Switzerland, Germany, United Kingdom, USA (1998). ISBN 0-87849-804-4.
- [12] M. M'Hamdi, H. Combeau, G. Lesoult: *International Journal of Numerical Methods for Heat & Fluid Flow*, 9 (1999), No. 3, 296–317.
- [13] *Foundation of Computational Thermodynamics: Thermo-Calc® Database Guide*. Thermo-Calc Software AB, Stockholm (2006).
- [14] W. J. Boettinger, J. A. Warren: *Metallurgical and Materials Transactions A*, 27A (1996), 657–669.
- [15] J. A. Warren, W. J. Boettinger: *Acta Metallurgica et Materialia*, 43 (1995), No. 2, 689–703.